



# SLICE: SPT-CL J0546-5345—A Prominent Strong-lensing Cluster at $z = 1.07$

Joseph F. V. Allingham<sup>1</sup>, Adi Zitrin<sup>1</sup>, Miriam Golubchik<sup>1</sup>, Lukas J. Furtak<sup>1</sup>, Matthew Bayliss<sup>2</sup>, Catherine Cerny<sup>3</sup>, Jose M. Diego<sup>4</sup>, Alastair C. Edge<sup>5,6</sup>, Raven Gassis<sup>2</sup>, Michael D. Gladders<sup>7,8</sup>, Mathilde Jauzac<sup>5,6,9,10</sup>, David J. Lagattuta<sup>5,6,11</sup>, Gavin Leroy<sup>6</sup>, Marceau Limousin<sup>12</sup>, Guillaume Mahler<sup>13</sup>, Ashish K. Meena<sup>1</sup>, Priyamvada Natarajan<sup>14,15</sup>, and Keren Sharon<sup>3</sup>

<sup>1</sup> Department of Physics, Ben-Gurion University of the Negev, P.O. Box 653, Be'er-Sheva 84105, Israel; [allingga@post.bgu.ac.il](mailto:allingga@post.bgu.ac.il)

<sup>2</sup> Department of Physics, University of Cincinnati, Cincinnati, OH 45221, USA

<sup>3</sup> Department of Astronomy, University of Michigan, 1085 South University Avenue, Ann Arbor, MI 48109, USA

<sup>4</sup> Instituto de Física de Cantabria (CSIC-UC). Avda. Los Castros s/n. 39005 Santander, Spain

<sup>5</sup> Centre for Extragalactic Astronomy, Department of Physics, Durham University, South Road, Durham DH1 3LE, UK

<sup>6</sup> Institute for Computational Cosmology, Durham University, South Road, Durham DH1 3LE, UK

<sup>7</sup> Kavli Institute for Cosmological Physics, University of Chicago, 5640 South Ellis Avenue, Chicago, IL 60637, USA

<sup>8</sup> Department of Astronomy and Astrophysics, University of Chicago, 5640 South Ellis Avenue, Chicago, IL 60637, USA

<sup>9</sup> Astrophysics Research Centre, University of KwaZulu-Natal, Westville Campus, Durban 4041, South Africa

<sup>10</sup> School of Mathematics, Statistics & Computer Science, University of KwaZulu-Natal, Westville Campus, Durban 4041, South Africa

<sup>11</sup> Centre for Astrophysics Research, Department of Physics, Astronomy and Mathematics, University of Hertfordshire, Hatfield AL10 9AB, UK

<sup>12</sup> Aix Marseille Univ, CNRS, CNES, LAM, Marseille, France

<sup>13</sup> STAR Institute, Quartier Agora - Allée du six Août, 19c B-4000 Liège, Belgium

<sup>14</sup> Department of Astronomy, Yale University, New Haven, CT 06511, USA

<sup>15</sup> Department of Physics, Yale University, New Haven, CT 06511, USA

Received 2025 July 11; revised 2025 August 3; accepted 2025 August 8; published 2025 August 29

## Abstract

Massive galaxy clusters act as prominent strong lenses. Due to a combination of observational biases, cluster evolution, and lensing efficiency, most of the known cluster lenses lie typically at  $z_l \sim 0.2\text{--}0.7$ , with only a few prominent examples at higher redshifts. Here we report the first strong-lensing analysis of the massive galaxy cluster SPT-CL J0546-5345 at a redshift  $z_l = 1.07$ . This cluster was first detected through the Sunyaev–Zel'dovich effect, with a high estimated mass for its redshift of  $M_{200,c} = (7.95 \pm 0.92) \times 10^{14} M_\odot$ . Using recent JWST/NIRCam and archival Hubble Space Telescope imaging, we identify at least 10 secure and 6 candidate sets of multiply imaged background galaxies, which we use to constrain the mass distribution in the cluster. We derive effective Einstein radii of  $\theta_E = 18.^{\prime\prime}1 \pm 1.^{\prime\prime}8$  for a source at  $z_s = 3$  and  $\theta_E = 27.^{\prime\prime}9 \pm 2.^{\prime\prime}8$  for a source at  $z_s = 9$ . The total projected mass within a 200 kpc radius around the strong-lensing region is  $M(<200 \text{ kpc}) = (1.9 \pm 0.3) \times 10^{14} M_\odot$ . While our results rely on photometric redshifts warranting spectroscopic follow-up, this central mass resembles that of the Hubble Frontier Fields clusters—although SPT-CL J0546-5345 is observed when the Universe was  $\sim 3\text{--}4$  Gyr younger. Amongst the multiply imaged sources, we identify a hyperbolic-umbilic-like configuration, and, thanks to its point-like morphology, a possible active galactic nucleus (AGN). If confirmed spectroscopically, it will add to just a handful of other quasars and AGN known to be multiply lensed by galaxy clusters.

*Unified Astronomy Thesaurus concepts:* Galaxy clusters (584); High-redshift galaxy clusters (2007); Strong gravitational lensing (1643); Gravitational lensing (670); Active galactic nuclei (16)

## 1. Introduction

The structure in the Universe is believed to grow hierarchically, with smaller structures forming first, later coalescing to form larger structures (e.g., I. B. Zeldovich et al. 1982; V. Springel et al. 2005). As the largest and most massive gravitationally bound objects in the Universe, galaxy clusters form late in cosmic history, around  $z \sim 3$ , when the Universe was about 2 Gyr old (e.g., A. V. Kravtsov & S. Borgani 2012; S. Planelles et al. 2015).

Dedicated imaging campaigns, with the Hubble Space Telescope targeting massive galaxy clusters, have revealed that they act as prolific gravitational lenses (e.g., CLASH, M. Postman et al. 2012; A. Zitrin et al. 2015; Hubble Frontier Fields, J. M. Lotz et al. 2017; RELICS, D. Coe et al. 2019; BUFFALO, C. L. Steinhardt et al. 2020). The lensing

efficiency of clusters depends on various factors such as their redshift, their mass, and its distribution. Lensing is dictated by the projected mass density such that more evolved clusters that are typically more concentrated, as well as those elongated along the line of sight, tend to show more prominent lensing features and exhibit large critical areas (A. Zitrin et al. 2013). It has also been shown that massive, merging clusters tend to show accentuated lensing properties, owing to the various massive substructures that together form a larger lens (e.g., M. Meneghetti et al. 2003; A. Zitrin et al. 2017; M. Jauzac et al. 2019; G. Mahler et al. 2019; A. Acebron et al. 2020; L. J. Furtak et al. 2023b).

Given the above, most well-known lensing clusters typically lie at redshifts  $z_l \gtrsim 0.2$ , below which the lensing efficiency becomes substantially weaker as the extended lens gets too close to the observer, and  $z_l \lesssim 0.7$ . This upper empirical “limit” is a result of various factors including cluster evolution, the change in lensing efficiency with redshift, and the typical observational depths. Also, a source sitting closely behind a  $z_l \sim 1$  cluster would not be efficiently lensed but may be



Original content from this work may be used under the terms of the [Creative Commons Attribution 4.0 licence](#). Any further distribution of this work must maintain attribution to the author(s) and the title of the work, journal citation and DOI.

prominently lensed by lower-redshift clusters (see, e.g., the giant arc in Abell 370, J. Richard et al. 2010), making these lenses easier to identify. Deeper or longer-wavelength surveys, such as those enabled by JWST, are needed to detect the bulk of high-redshift galaxies that are possibly lensed by high-redshift clusters.

In addition, massive lensing clusters are often optically, near-infrared (e.g., M. D. Gladders & H. K. C. Yee 2005; E. S. Rykoff et al. 2014), or X-ray selected (e.g., H. Ebeling et al. 2010), which also limits their redshift range. In that respect, Sunyaev-Zel'dovich effect (SZE) surveys have the potential to detect higher-redshift clusters given the (relative) insensitivity of SZE to redshift. Indeed, surveys with the Planck spacecraft (Planck Collaboration et al. 2011), South Pole Telescope (SPT; L. E. Bleem et al. 2015), and Atacama Cosmology Telescope (M. Hilton et al. 2021) have detected numerous such candidates.

The massive galaxy cluster SPT-CL J0546-5345 was first discovered through the SZE with the SPT (Z. Staniszewski et al. 2009; K. Vanderlinde et al. 2010). M. Brodwin et al. (2010) measured a cluster redshift of  $\langle z_l \rangle = 1.067$ , making SPT-CL J0546-5345 the first  $z > 1$  cluster discovered by the SZE. Combining velocity dispersion with X-ray, SZE, and richness measures, they derived a high mass approaching  $M_{200,c} \sim 1 \times 10^{15} M_\odot$  (see also S. Abdulshafy et al. 2025). While some lensing features were noted in imaging data as early as Z. Staniszewski et al. (2009), SPT-CL J0546-5345 has never been, to our knowledge, subject to strong lens modeling.

Here, we present a first strong-lensing analysis of the cluster, now enabled thanks to new JWST observations from the Strong Lensing and Cluster Evolution program (SLICE; JWST Cycle 3 GO-05594, PI: Mahler; G. Mahler et al. 2025, in preparation; C. Cerny et al. 2025), along with archival Hubble Space Telescope (HST) and ground-based data. Our work adds to a recent analysis that included four  $z \in [0.8; 1.06]$  clusters presented in C. Cerny et al. (2025) and several other strong-lensing galaxy clusters around  $z_l \sim 1$  analyzed in past years (see, e.g., A. Zitrin et al. 2015; R. Paterno-Mahler et al. 2018; G. Mahler et al. 2020; J. M. Diego et al. 2023; G. Smith et al. 2025).

This work is organized as follows: in Section 2, we describe the data used in this work. In Sections 3 and 4, we describe the analysis of the cluster and discuss the results, respectively. Our conclusion is presented in Section 5. Throughout this Letter, we use a standard flat  $\Lambda$ CDM cosmology with  $H_0 = 70 \text{ km s}^{-1} \text{ Mpc}^{-1}$ ,  $\Omega_\Lambda = 0.7$ , and  $\Omega_m = 0.3$ . With these parameters,  $1''$  at the redshift of the cluster corresponds to 8.12 kpc. Magnitudes are quoted in the AB system (J. B. Oke & J. E. Gunn 1983), and all quoted uncertainties represent  $1\sigma$  ranges unless stated otherwise.

## 2. Data

### 2.1. Imaging and spectroscopy

SPT-CL J0546-5345 was observed with JWST in Cycle 3 (Program ID: GO-5594; PI: G. Mahler) with the NIRCam (M. J. Rieke et al. 2023). These observations comprise 1836 s of observing time in both F150W2 and F322W2, taken simultaneously. While SLICE performs in-house dedicated data reduction (G. Mahler et al. 2025, in preparation; C. Cerny et al. 2025), for the current work, we use the data reduced using the Grism redshift and line analysis software for space-

based slitless spectroscopy (`grizli`, G. Brammer et al. 2022)<sup>16</sup> as downloaded from the DAWN JWST Archive (DJA).<sup>17</sup> These observations are complemented with HST observations from WFC3 (Cycle 25, Program ID: GO-15294; PI: G. Wilson), amounting to a total of 5623.5 s integration with the F160W broadband filter, and from ACS (Cycle 19, Program ID: GO-12477; PI: F. High), for a total of 1920 s integration with the F606W and 1916 s with the F814W broadband filters, respectively. The F814W and F160W data are retrieved through the DJA together with the JWST data. The F606W data were not included in the DJA, and we retrieve them from the MAST archive directly and align them onto the same pixel grid as the JWST (and other HST) data using the software `SWarp` (E. Bertin et al. 2002). There also exists Very Large Telescope/VIMOS imaging in the  $U, B, R$ , and  $I$  bands (program 097.A-0734, PI: R. Demarco), for  $\sim 1500$ –4000 s in each band, of which we make use here to further aid or cast confidence, mostly on a by-eye basis, in the multiple image and cluster member selections.

Spectroscopic measurements are reported in the literature for this cluster, although none for the multiply imaged sources we identify here. M. Brodwin et al. (2010) first confirmed spectroscopically 18 early-type cluster members with the IMACS/GISMO instrument on the Magellan Baade telescope (A. Dressler et al. 2011). J. Ruel et al. (2014), C. Sifón et al. (2016), S. M. Sweet et al. (2017), T. Schrabback et al. (2018), and M. L. Balogh et al. (2021) continued the spectroscopic analysis of the cluster with observations from, e.g., GMOS, FORS2, IMACS, low-dispersion survey spectrograph 3, and SALT/RSS, amounting to a total of  $\sim 100$  spectroscopic cluster member detections. We use a compilation of these spectroscopic redshifts to validate our cluster member selection (Section 2.2).

Some other relevant data exist for the cluster, although not explicitly used here. For example, P. Aguirre et al. (2018) and J. F. Wu et al. (2018) identified a population of dusty star-forming galaxies in the cluster background, using a combination of Atacama Large Millimeter/submillimeter Array (ALMA), APEX/LABOCA, ACTA, and the PACS and Spire instruments of the Herschel Space Telescope. Finally, D. G. Phuravhathu et al. (2025) concluded from MeerKAT observations coupled with Chandra that SPT-CL J0546-5345 exhibits a mostly relaxed morphology.

### 2.2. Cluster Member Galaxies

We build a photometric catalog for the cluster using the software `SExtractor` (E. Bertin & S. Arnouts 1996) from all HST and JWST filters available. As these are the starting point of the lens model (see Section 3), we aim to extract a catalog of cluster member galaxies. To that end, we follow the red-sequence method (M. D. Gladders & H. K. C. Yee 2000). We construct a color–magnitude diagram using the ACS/F814W and WFC3/F160W bands (at the cluster's redshift, the break around rest frame  $\sim 4000 \text{ \AA}$  falls in the middle of the F814W filter). After fitting the main sequence of galaxies down to 23 AB magnitude, we choose sources within 0.5 mag from the fitted line. We then check the validity of the selection by comparing it to the list of spectroscopically confirmed cluster members (see Section 2.1). We further refine the

<sup>16</sup> <https://github.com/gbrammer/grizli>

<sup>17</sup> <https://dawn-cph.github.io/dja/imaging/v7/>

catalog using a by-eye inspection of the image to detect spurious or missing galaxies that appear to be cluster members. Our final selection includes 160 cluster member galaxies. We take the F814W magnitude as reference in the associated lens modeling mass–luminosity scaling relation.

### 2.3. Photometric Redshift Measurements

Photometric redshifts, especially in the absence of spectroscopic redshifts for most background sources, can help in the identification of multiply imaged systems and are needed to estimate the sources’ redshifts for the lens modeling. Here we use the spectral-energy-distribution fitting software *Bagpipes* (see A. C. Carnall et al. 2018), modified with custom stellar libraries from G. Bruzual & S. Charlot (2003), to obtain photometric redshifts for multiple image candidates. We adopt a constant star formation history (SFH) and a lower limit on redshift of  $z = 1.2$ . We note that there are only five wide imaging bands, which renders these photometric redshift measurements uncertain and emphasizes the need for a spectroscopic follow-up of the cluster.

In Figure 1, we show a color-composite image of the cluster, where there appears to be a green artifact from the NIRCam/F150W2 band. The effect of this artifact on the photometric redshift measurement should be negligible, given the local background subtraction. To test this explicitly, we rerun the photometric redshift estimation while introducing a baseline 20% error on NIRCam/F150W2 measurements in the relevant region. This yields photometric redshifts well within  $1\sigma$  of results reported in Table 1.

## 3. Lensing Analysis

We use here the Light-Traces-Mass (LTM) modeling method developed by A. Zitrin et al. (2009, 2015; see also T. Broadhurst et al. 2005). This method has been extensively used on large samples of clusters, and thanks to the assumption that light traces mass, excels in matching up multiply imaged galaxies even before a model is fully minimized. It is thus a powerful method in particular for newly analyzed clusters. The multiple image matching is performed by constructing an initially well-guessed model (using only the photometry of cluster members) and then delensing-reレンズing arclets to predict the observed appearance of counterimages, which are then searched for in the observations. The method is described in greater detail in A. Zitrin et al. (2015), and we briefly summarize it here.

The model is composed of three components. First, a map of cluster galaxies is constructed by assigning a power-law mass density profile to each galaxy, where the exponent is a free parameter of the model. The exponent is the same for all galaxies, and the mass (or weight) of each galaxy is scaled in proportion to its luminosity. The mass distribution of each galaxy is assumed to be circular, except the western Brightest Cluster Galaxy (BCG) here, whose ellipticity is set to the measured values from SExtractor. Then, a dark matter map is constructed by smoothing the resulting map of cluster galaxies, using a Gaussian kernel whose width is also a free parameter of the model. The relative weight between the galaxy and dark matter components, and the overall normalization, are free parameters in the model as well. Finally, an external shear is added, which allows for more freedom, introducing effective ellipticity to the model. In addition, we also leave here the weight (i.e., mass normalization) of key bright galaxies free to be optimized by the model—these are marked in Figure 1. It is important to note that none of the lensed

galaxies or multiple image systems we find here has a spectroscopic redshift measurement. Since the exact redshifts of the lensed galaxies are unknown, we adopt, as an initial guide, their photometric redshift estimates but allow their redshift to be optimized by the model using a wide prior. In practice, this is done through a uniformly distributed prior range on the distance ratio,  $D_{\text{LS}}/D_s$ , typically spanning the redshift range from  $z \sim 1.5$ –2 to  $z \gtrsim 6$ , where  $D_{\text{LS}}$  and  $D_s$  are the angular-diameter distances between the lens and source, and to the source, respectively.

Once multiple image systems are iteratively found using a set of preliminary lens models, as well as color, symmetry, appearance, and photometric redshift information, a final model is constructed. The model is optimized using Markov Chain Monte Carlo, minimizing the  $\chi^2$  function that quantifies the distance between the predicted positions of multiple images and their observed positions.

Because LTM needs to be anchored (i.e., scaled) to a reference redshift, we choose System 3 (see Figure 1 and Table 1) for its robust photometric redshift estimate and because it is well distributed across the cluster field. We anchor  $z_3 = 3.5$  as estimated using the photometric redshift results (see Table 1). To account for the uncertainty in the redshift of the system, we use two other identical setup models but anchored at  $z_3 = 3.25$  and 3.75 following the  $1\sigma$  photometric redshift uncertainty of  $\Delta z = 0.25$ . All uncertainties derived hereafter take this propagated uncertainty into account.

## 4. Results and Discussion

### 4.1. Mass Model

We mark the identified multiple image systems and the critical curves derived from the best-fit model on Figure 1. In total, we detect 35 multiple images and a few additional candidates, belonging to at least 10 background sources (some systems, such as System 6, contain clumps that may, in principle, be separate galaxies). All securely identified images of these 10 systems were used to constrain the lens model, with the exception of System 7, which was optimized with System 6 (see Section 4.2); this amounts to 30 images used as constraints. We also identify 6 other candidate systems, comprising 16 multiple image candidates, which can be confirmed with spectroscopic follow-up.

The large number of systems, and the prominent lensing features seen in Figure 1, are rather surprising for a  $z_l > 1$  cluster and show its importance. The model was minimized using 39 constraints and 28 free parameters, resulting in 11 degrees of freedom. The final model has a reduced  $\chi^2 \simeq 68/11$  and an  $rms \simeq 1.^{\circ}2$  in reproducing the multiple images. While slightly larger than typical high-end parametric lens models (e.g., J. Richard et al. 2014; R. Kawamata et al. 2016; L. J. Furtak et al. 2024b), this is typical (and in fact quite low) for LTM models, especially for such complex clusters (e.g., A. Zitrin et al. 2017; A. Acebron et al. 2020). Given it is coupled to the light distribution, the LTM methodology is less flexible on one hand, resulting in a somewhat higher  $rms$  as seen here, but on the other hand, allows for a strong, initial prediction power (M. Carrasco et al. 2020; L. Zalesky & H. Ebeling 2020), particularly useful for complex clusters analyzed for the first time (e.g., A. Zitrin et al. 2017). We make our resulting lens model publicly available.<sup>18</sup>

<sup>18</sup> doi:10.5281/zenodo.16534337

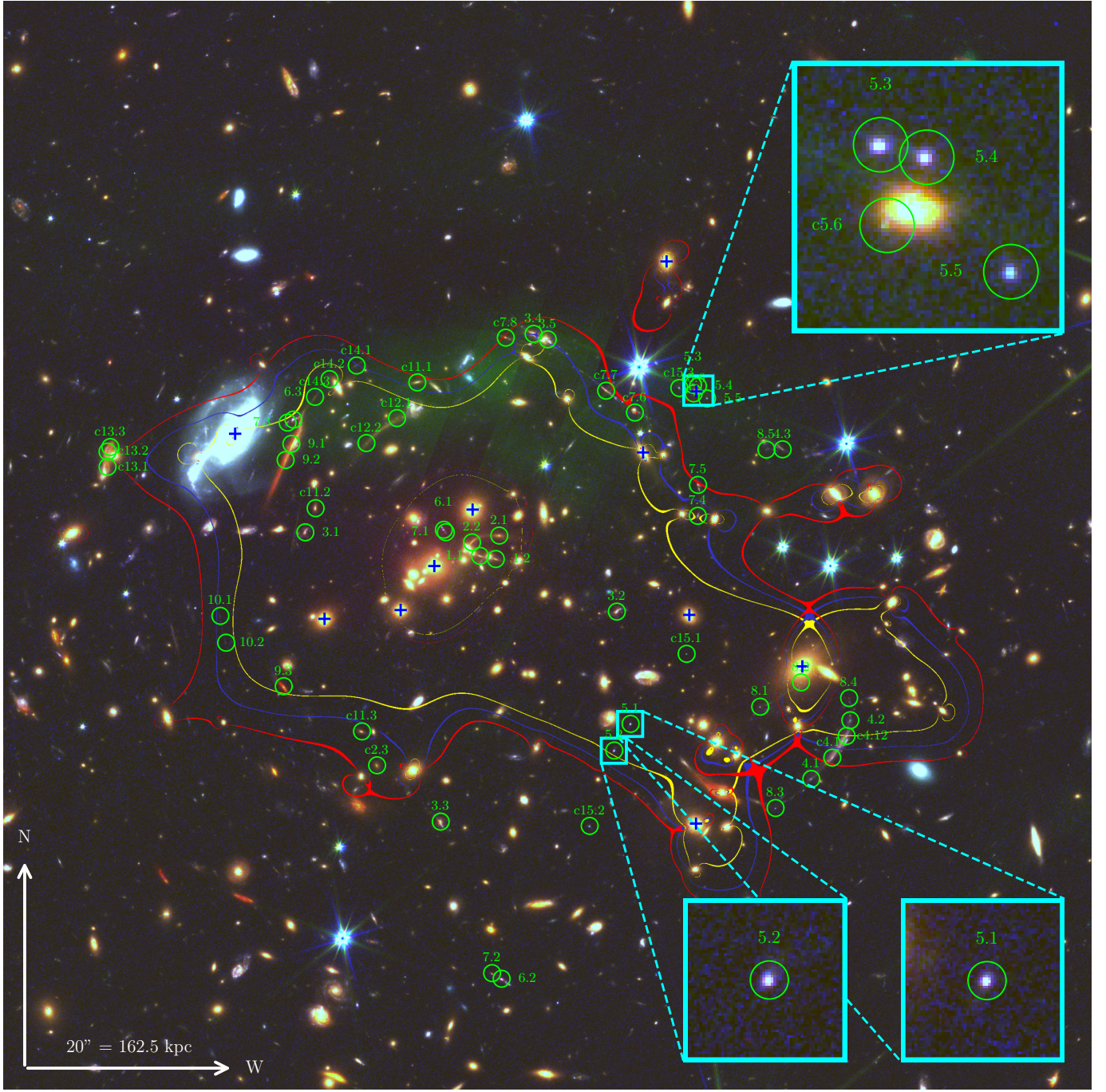


**Figure 1.** Color-composite image of SPT-CL J0546-5345 constructed from SLICE JWST and archival HST imaging of the cluster (red: F322W2; green: F150W2; blue: F814W). Strong-lensing multiple images are numbered and labeled in green. The yellow, blue, and red lines represent, respectively, the critical curves for source redshifts  $z_s = 3.5$  (System 3),  $z_s = 4.5$ , and  $z_s = 6$ , as computed from our strong-lensing model of the cluster. Galaxies left freely weighted in the modeling are marked with crosses. Highlighted in cyan squares are the images of System 5, the multiply imaged point-like nucleus—and potential AGN—reported in this work. Note that an artifact from the F150W2 band appears in green north of the cluster core. This is cosmetic only, and we verified that it has no substantial effect on our results (see Section 2.3).

The mass density distribution in units of the critical density for lensing and the magnification maps are both shown in Figure 2. The critical curves for sources at redshifts  $z_s = 2$ ,  $3$ , and  $9$  enclose, respectively, areas of  $\mathcal{A}_{z_s=2} = 0.09 \pm 0.02$  arcmin $^2$ ,  $\mathcal{A}_{z_s=3} = 0.28 \pm 0.06$  arcmin $^2$ , and  $\mathcal{A}_{z_s=9} = 0.68 \pm 0.13$  arcmin $^2$ . These correspond, respectively, to effective Einstein radii of  $\theta_{E,z_s=2} = 10.^{\circ}0 \pm 1.^{\circ}0$ ,  $\theta_{E,z_s=3} = 18.^{\circ}1 \pm 1.^{\circ}8$ , and  $\theta_{E,z_s=9} = 27.^{\circ}9 \pm 2.^{\circ}8$ . The  $z_s = 2$ ,  $3$ , and  $9$  critical curves enclose projected masses, respectively, of  $M(\in \mathcal{A}_{z_s=2}) = (6.1 \pm 0.9) \times 10^{13} M_\odot$ ,  $M(\in \mathcal{A}_{z_s=3}) = (1.4 \pm 0.2) \times 10^{14} M_\odot$ , and  $M(\in \mathcal{A}_{z_s=9}) = (2.6 \pm 0.4) \times 10^{14} M_\odot$ .

( $6.1 \pm 0.9) \times 10^{13} M_\odot$ ,  $M(\in \mathcal{A}_{z_s=3}) = (1.4 \pm 0.2) \times 10^{14} M_\odot$ , and  $M(\in \mathcal{A}_{z_s=9}) = (2.6 \pm 0.4) \times 10^{14} M_\odot$ .

The total projected (cylindrical) mass density enclosed within 200 kpc from the cluster center, defined here between the two main mass clumps, i.e., (R.A.; decl.) = (86.6486467;  $-53.7599104$ ) deg, is  $M(<200 \text{ kpc}) = (1.9 \pm 0.3) \times 10^{14} M_\odot$  and within 500 kpc,  $M(<500 \text{ kpc}) = (6.5 \pm 1.0) \times 10^{14} M_\odot$ . This former mass is similar to that of typical massive lensing clusters usually observed at lower redshifts (see, e.g., C. Fox

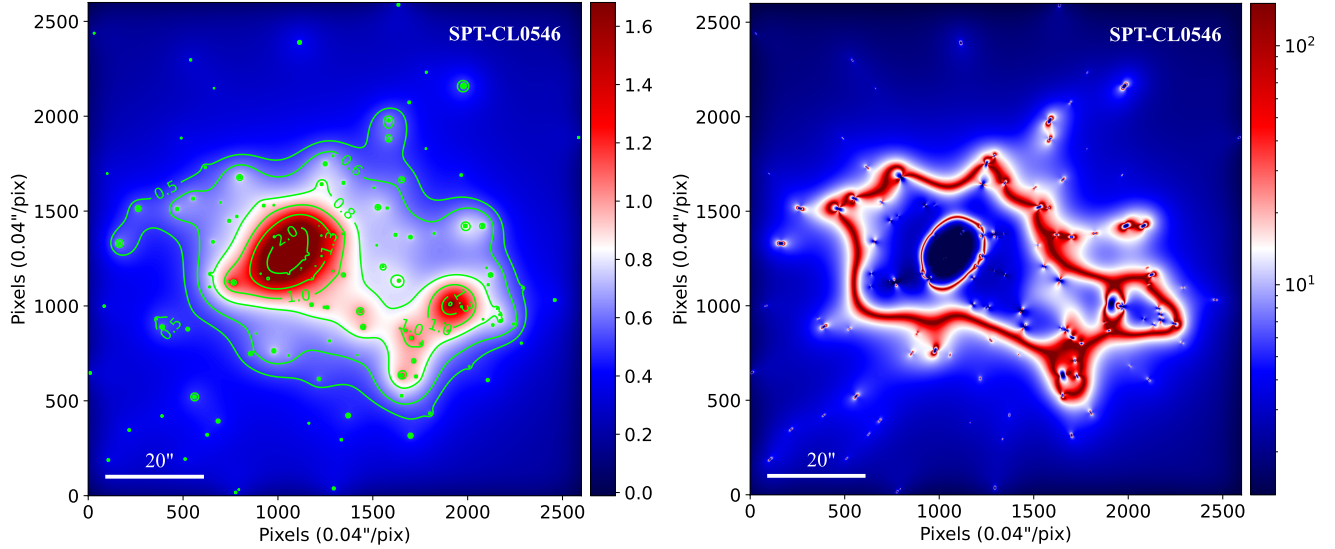


**Figure 2.** Surface mass density map (left), in units of the critical density for lensing, and magnification map (right), both for an assumed source redshift of  $z_s = 3.5$ , from the best-fit LTM model.

**Table 1**  
Multiple Images and Candidates

Arc ID (1)	R.A. (2)	Decl. (3)	$z_{\text{phot}}^{50\%}$ [16%–84%] (4)	$z_{\text{model}}$ [16%–84%] (5)	Comments (6)
1.1	05:46:37.1684	-53:45:29.876	...	2.76 [2.58–2.79]	Relensed images predicted in the west, maybe corresponding to System 11
1.2	05:46:36.9976	-53:45:30.179	...		Relensed images predicted in the west, maybe corresponding to System 11
2.1	05:46:36.9549	-53:45:27.906	1.58 [1.33–1.95]	1.73 [1.72–1.94]	...
2.2	05:46:37.2526	-53:45:28.578	...		...
c2.3	05:46:38.2754	-53:45:49.833	1.65 [1.35–2.07]		The relensed image corresponds with c2.3
3.1	05:46:39.0491	-53:45:27.604	3.47 [3.21–3.78]	3.50 [3.25–3.75] <sup>a</sup>	...
3.2	05:46:35.6897	-53:45:35.207	3.51 [3.23–3.85]		...
3.3	05:46:37.5895	-53:45:55.317	3.47 [3.23–3.75]		...
3.4	05:46:36.5909	-53:45:08.624	3.48 [3.25–3.75]		...
3.5	05:46:36.4313	-53:45:09.137	...		...
4.1	05:46:33.5957	-53:45:51.184	1.85 [1.40–3.34]	3.76 [3.31–3.87]	...
4.2	05:46:33.1748	-53:45:45.583	1.72 [1.37–2.91]		Possible ALMA continuum detection (J. F. Wu et al. 2018)
4.3	05:46:33.9035	-53:45:19.681	1.86 [1.43–2.64]		Possible ALMA continuum detection (J. F. Wu et al. 2018)
c4.11	05:46:33.3698	-53:45:49.174	2.31 [1.46–3.37]	...	...
c4.21	05:46:33.2156	-53:45:47.095	"	...	...
5.1	05:46:35.5420	-53:45:45.915	3.29 [2.16–3.58]	3.41 [3.22–3.44]	AGN candidate
5.2	05:46:35.7182	-53:45:48.462	3.25 [2.58–3.58]		AGN candidate
5.3	05:46:34.8683	-53:45:13.497	3.14 [2.16–3.58]		AGN candidate
5.4	05:46:34.8157	-53:45:13.621	3.01 [1.97–3.44]		AGN candidate
5.5	05:46:34.7178	-53:45:14.797	2.95 [2.16–3.45]		AGN candidate
c5.6	05:46:34.8619	-53:45:14.292	...		Fainter candidate AGN image
6.1	05:46:37.5542	-53:45:27.352	5.03 [4.78–5.25]	6.94 [6.21–7.06]	...
6.2	05:46:36.9310	-53:46:10.274	5.01 [4.92–5.10]		...
6.3	05:46:39.1766	-53:45:16.814	4.90 [4.79–5.03]		...
7.1	05:46:37.5350	-53:45:27.571	...	6.94 [6.21–7.06]	Optimized with System 6
7.2	05:46:37.0333	-53:46:09.754	5.65 [1.61–6.19]		Optimized with System 6
7.3	05:46:39.2391	-53:45:17.106	3.59 [2.95–4.11]		Optimized with System 6
7.4	05:46:34.8151	-53:45:25.998	5.03 [4.30–5.23]		Optimized with System 6
7.5	05:46:34.8151	-53:45:23.047	5.43 [5.15–5.66]		Optimized with System 6
c7.6	05:46:35.4921	-53:45:16.163	...		Optimized with System 6, images c7.6–c7.8 form a very long arc which consists likely of counterimages of systems 6+7; exact configuration unclear
c7.7	05:46:35.8078	-53:45:14.014	5.44 [1.35–5.99]		Optimized with System 6, images c7.6–c7.8 form a very long arc which consists likely of counterimages of systems 6+7; exact configuration unclear
c7.8	05:46:36.8846	-53:45:08.964	6.07 [1.77–6.99]		Optimized with System 6, images c7.6–c7.8 form a very long arc which consists likely of counterimages of systems 6+7; exact configuration unclear

**Table 1**  
(Continued)

Arc ID (1)	R.A. (2)	Decl. (3)	$z_{\text{phot}}^{50\%}$ [16%–84%] (4)	$z_{\text{model}}$ [16%–84%] (5)	Comments (6)
8.1	05:46:34.1448	−53:45:44.274	2.25 [1.63–3.32]	3.99 [3.51–4.00]	Hyperbolic-umbilic-like system; system may be related to System 4
8.2	05:46:33.7016	−53:45:41.942	...		Hyperbolic-umbilic-like system; system may be related to System 4
8.3	05:46:33.9781	−53:45:53.970	2.68 [1.69–3.43]		Hyperbolic-umbilic-like system; system may be related to System 4
8.4	05:46:33.1879	−53:45:43.434	...		Hyperbolic-umbilic-like system; system may be related to System 4
8.5	05:46:34.0748	−53:45:19.680	...		Hyperbolic-umbilic-like system; system may be related to System 4
9.1	05:46:39.1740	−53:45:19.026	3.58 [3.31–3.84]	2.88 [2.88–3.01]	A known, dusty, star-forming galaxy; ALMA detected (J. F. Wu et al. 2018)
9.2	05:46:39.2523	−53:45:20.672	...		A known, dusty, star-forming galaxy; ALMA detected (J. F. Wu et al. 2018)
9.3	05:46:39.2773	−53:45:42.406	3.52 [2.01–4.12]		...
10.1	05:46:39.9678	−53:45:35.575	...	3.70 [3.53–3.74]	...
10.2	05:46:39.9047	−53:45:38.160	...		...
c11.1	05:46:37.8396	−53:45:13.256	1.76 [1.37–2.58]	...	May be counterimaged with system 1
c11.2	05:46:38.9357	−53:45:25.280	1.78 [1.44–2.56]	...	May be counterimaged with system 1
c11.3	05:46:38.4399	−53:45:46.624	1.80 [1.43–2.52]	...	May be counterimaged with system 1
c12.1	05:46:38.1034	−53:45:17.095	2.15 [1.59–2.89]	...	$z_{\text{phot}}$ of 12.1 was measured on the arc, between the two clumps 12.1 and 12.2
c12.2	05:46:38.3263	−53:45:18.535	2.14 [1.86–2.48]	...	$z_{\text{phot}}$ of 12.1 was measured on the arc, between the two clumps 12.1 and 12.2
c13.1	05:46:41.2089	−53:45:21.101	2.92 [1.85–3.15]	...	Galaxy–galaxy strong lensing, $z_{\text{phot}}$ for 13.1 was measured on the nearby nucleus
c13.2	05:46:41.1951	−53:45:19.834	...	...	Galaxy–galaxy strong lensing
c13.3	05:46:41.1794	−53:45:19.532	...	...	Galaxy–galaxy strong lensing
c14.1	05:46:38.5037	−53:45:11.698	...	...	...
c14.2	05:46:38.7812	−53:45:12.904	...	...	...
c14.3	05:46:38.9436	−53:45:14.746	...	...	...
c15.1	05:46:34.9388	−53:45:39.220	...	...	...
c15.2	05:46:35.9804	−53:45:55.658	1.83 [1.40–3.48]	...	...
c15.3	05:46:35.0187	−53:45:13.800	1.68 [1.32–3.18]	...	...

**Notes.** Column (1): arc ID. “c” stands for candidate where identification was more ambiguous or if the image was not used as constraint. Columns (2) and (3): R.A. and decl. in J2000.0. Column (4): photometric redshift 50th [16%–84%] percentiles from Bagpipes. Column (5): predicted and 64% C.I. redshift by our LTM lens model, for systems whose redshift was left to be optimized in the minimization. Column (6): comments. For systems 12 and 13, some images were not identified in the photometric catalog, and thus, we quote a photometric redshift for a nearby clump or region from the same arc, as also mentioned in the relevant comments column.

<sup>a</sup> All the uncertainties on model redshifts and across this Letter take into account the  $1\sigma$  redshift uncertainty for System 3 ( $z_s = 3.5 \pm 0.25$ ) by running three different mass models, anchored at  $z_s = 3.25, 3.5$ , and  $3.75$ .

et al. 2022), including the Hubble Frontier Fields (HFF) sample for which  $M$  ( $<200$  kpc) is in the range  $(1.5\text{--}2.3) \times 10^{14} M_\odot$ , even though these are observed when the Universe is  $\sim 3\text{--}4$  Gyr older.

In order to compare with previous mass measurements of this cluster by other probes such as from X-ray and SZE data, or from a previous HST weak-lensing analysis, we fit a spherical Navarro–Frenk–White (NFW) profile (J. F. Navarro et al. 1996) to the best-fit model density profile. We obtain an extrapolated (3D) mass of  $M_{500,c}^{\text{SL,NFW}} = (7.2 \pm 0.5) \times 10^{14} M_\odot$ .<sup>19</sup> The X-ray, SZE, and weak-lensing masses reported in the literature in a similar radius are  $M_{500}^X = (5.33 \pm 0.62) \times 10^{14} M_\odot$  (K. Andersson et al. 2011),  $M_{500}^{\text{SZ}} = (5.05 \pm 0.82) \times 10^{14} M_\odot$  (K. Vanderlinde et al. 2010), and  $M_{500}^{\text{WL}} = (3.7_{-2.3}^{+2.6} \pm 0.8 \pm 0.5) \times 10^{14} M_\odot$ , (T. Schrabback et al. 2018), respectively. As this comparison is based on many assumptions (extrapolation, spherical symmetry, NFW profile, and hydrostatic equilibrium of the intracluster medium), a variety of factors, such as projection effects or nonthermal

pressure, may explain this apparent few  $\sigma$  scatter between the different measurements (M. Meneghetti et al. 2010; E. Rasia et al. 2012; D. Martizzi & H. Agrusa 2016). For comparison, the hydrostatic-to-lensing mass ratio (or bias) we find for  $M_{500}^{\text{HSE}}/M_{500}^{\text{Lens}} = 0.74$  is similar to the one found by M. Muñoz-Echeverría et al. (2024) for a sample of clusters at redshifts 0.05–1.07.

#### 4.2. A Few Spectacular Lensing Features

Some of the lensed sources show unique features. For instance, the prominent System 8 forms what appears to be a hyperbolic-umbilic configuration (a ring-shaped structure of four off-centered images and typically an additional outer image; see G. Orban de Xivry & P. Marshall 2009; D. J. Lagattuta et al. 2023; A. K. Meena & J. S. Bagla 2024), including a giant arc designated here as System 4 (see Figures 1 and 3). We note that Systems 4 and 8 may be two different parts of the same background galaxy. Similarly, System 11 may in fact consist of counterimages of System 1.

Also of interest, System 5 comprises an obvious nuclear point source, embedded in a very dim arc, multiply imaged five or six times where three of the images wrap a cluster galaxy forming an Einstein quad. The point-like appearance is

<sup>19</sup>  $M_{\Delta,c}$  is defined as the mass within a 3D sphere of radius  $R_\Delta$ , where the average density is  $\Delta \cdot \rho_c(z)$ , with  $\rho_c(z)$  being the critical density of the Universe at redshift  $z$ , i.e.,  $R_\Delta = \left\{ R \mid \frac{M(\leq R)}{(4/3)\pi R^3} = \Delta \cdot \rho_c(z) \right\}$ .

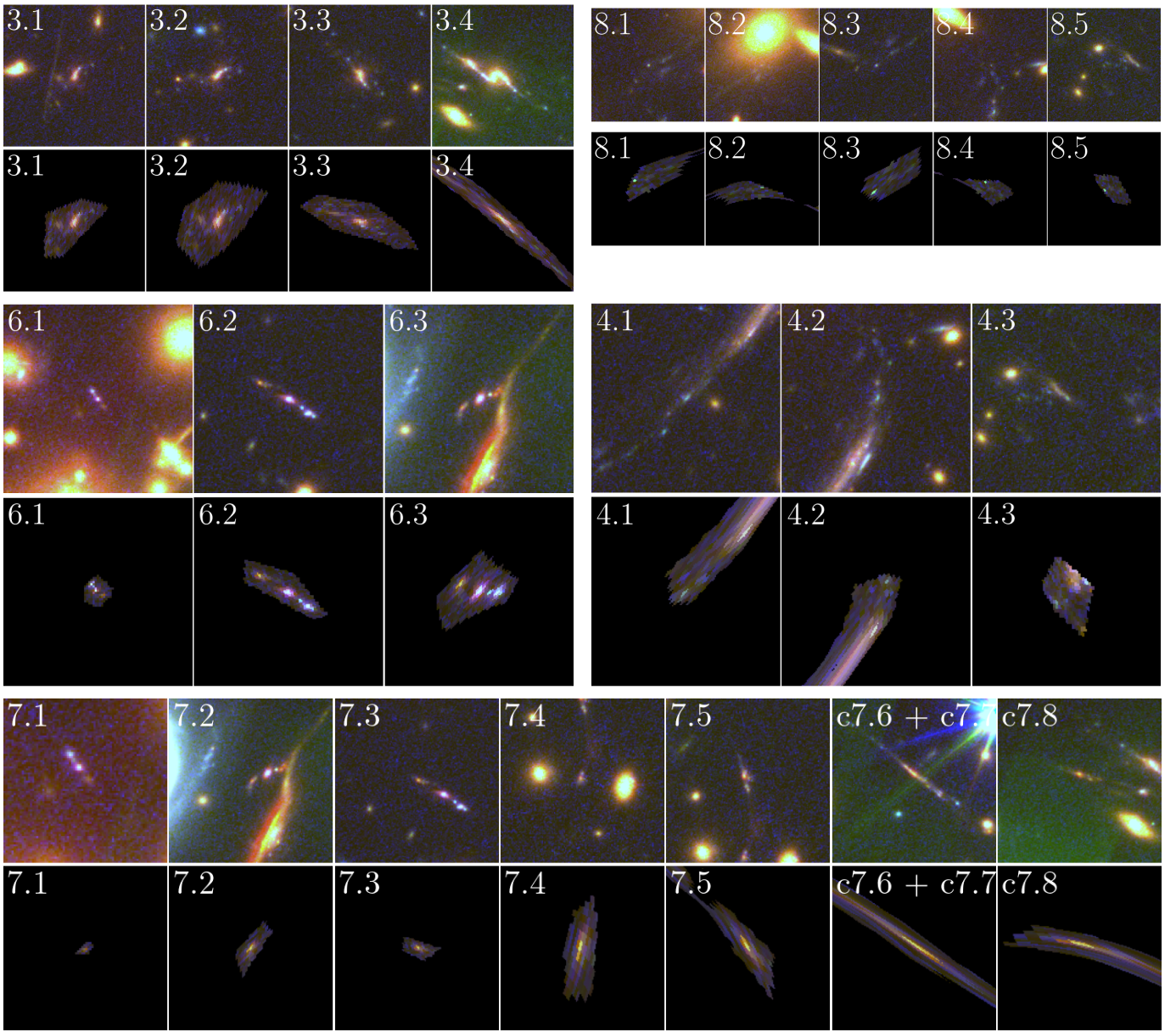


**Figure 3.** Reproduction of several systems by our model. For each system, we delens one image—typically the first one—to the source plane and back to the image plane, displaying the reproduction of the other images in that system. The upper row, for each system, shows the images as they appear in the red, green, and blue color image of the cluster (Figure 1), and the bottom row shows their reproduction by our model. As can be seen, the model does a very good job in reproducing the appearance of multiple images, strengthening their identification and showcasing its robustness.

reminiscent of other multiply imaged active galactic nuclei (AGN) detected in the same manner (e.g., L. J. Furtak et al. 2023a, 2024a). A zoom-in on the AGN candidate is displayed as an inset in Figure 1. Only a few galaxy-cluster-lensed multiply imaged AGN are known to date (A. P. Cloonan et al. 2025). If confirmed spectroscopically, this will supply another multiply imaged AGN with a range of time delays between its images that can then be used for measurements of the expansion rate of the Universe or for efficient reverberation mapping of supermassive black holes (e.g., P. R. Williams et al. 2021; K. Napier et al. 2023; M. Golubchik et al. 2024; X. Ji et al. 2025). Our lens model suggests that the Einstein cross images around the cluster member, i.e., images 5.3–5.6, arrive first within days or weeks of each other and about  $\sim 40$ – $50$  yr before the other two images (5.1 and 5.2), which are predicted to arrive weeks from one another. We leave a

more detailed investigation of the time delays to future works in case the AGN candidate is indeed confirmed to be a variable source.

Another system (System 9) is a very red dusty object, at  $z \sim 3$ , invisible in the optical HST data. System 7 is also remarkable, as some of its multiple images are lensed into a complex giant arc with very high magnifications, potentially allowing a uniquely zoomed-in view into the various stellar clumps seen therein (similar to other lensed clumps seen uniquely with JWST, e.g., E. Vanzella et al. 2023; M. Limousin et al. 2025). Given the complexity of the arc and the fact that it is much more magnified than the other counterimages of that system, it is hard to determine which substructures are counterimaged, and thus, we do not use this system as constraints and leave a more detailed investigation of this arc to future work. Nonetheless, as displayed in Figure 3, our lens

model naturally reproduces the arc, acting as another evidence for its robustness. More details on the specific images are given in Table 1.

### 4.3. An Uncommonly Massive Galaxy Cluster?

To get a sense of the rarity of the strong-lensing properties of the cluster, we compare its Einstein radius to a semianalytic calculation using a cosmological halo mass function. We adopt the J. Tinker et al. (2008) mass function and examine the expected number of lenses per given Einstein radius, in the redshift range  $z_l = 1\text{--}1.2$ . To do this, we run over the mass function in  $10^{14} M_\odot$  bins from  $10^{14}$  to  $3 \times 10^{15} M_\odot$  and over the above redshift range in  $\delta z = 0.1$  bins. For each redshift and for each mass bin, we calculate the distribution of Einstein radii (S. Sadeh & Y. Rephaeli 2008) by assuming an NFW halo (J. F. Navarro et al. 1996) for the clusters and adopting the concentration–mass relation and scatter from M. Meneghetti et al. (2014). The distribution of Einstein radii  $N(\theta_E)$  is then obtained by integrating over the comoving volume per each redshift bin and over all mass bins (for more details, see also M. Golubchik et al. 2024). The distribution is shown in Figure 4, where we show both the expected all-sky distribution and the same distribution normalized to the SPT survey area—with which SPT-CL J0546-5345 was first detected. We find that, at  $z_l \simeq 1.07$ , the largest observed Einstein radius across the sky should typically be of the same order as observed for SPT-CL J0546-5345, but the chances to find such a cluster in the SPT survey are much smaller, given the small fraction of the SPT survey area compared to the whole sky,  $\sim 0.06$ . This somewhat simplistic treatment has some obvious caveats. For instance, the adopted mass function is simulation based, and in addition, the small simulation volume is likely missing the largest clusters (W. A. Watson et al. 2014), and thus, the corresponding number density of large Einstein radii based on the mass function we adopt should be considered a lower limit. Moreover, our calculation does not take into account the lens ellipticity or merging state, and the  $c$ – $M$  relation may differ at higher redshifts. Nonetheless, the calculation generally shows that, indeed, such lensing configurations should be rare at  $z \gtrsim 1$ .

Nevertheless, several other distant lensing galaxy clusters that were analyzed in recent years show prominent lensing features and correspondingly, large central projected masses. For example, using similar data from the SLICE JWST survey, C. Cerny et al. (2025) modeled the galaxy clusters SPT-CL J0516-5755 ( $z_l = 0.966$ ) and SPT-CL J2011-5228 ( $z_l = 1.064$ ). These two clusters have Einstein radii of  $\theta_{E,z_s=2} = 6'' - 7''$  for a source at  $z_s = 2$  and  $\theta_{E,z_s=9} = 22'' - 33''$  for a source at  $z = 9$ . For comparison, our present analysis of SPT-CL J0546-5345 yields Einstein radii of  $\theta_{E,z_s=2} = 10.0 \pm 1.0$  and  $\theta_{E,z_s=9} = 27.9 \pm 2.8$ , respectively, i.e., displaying similar or stronger lensing properties. The enclosed 2D projected mass within 500 kpc found by C. Cerny et al. (2025) for these two clusters is  $M(<500 \text{ kpc}) = 5.10_{-0.18}^{+0.42} \times 10^{14} M_\odot$  and  $7.73_{-0.00}^{+1.75} \times 10^{14} M_\odot$ , respectively, i.e., similar to the  $M(<500 \text{ kpc}) = (6.5 \pm 1.0) \times 10^{14} M_\odot$  we find here for SPT-CL J0546-5345.

Other examples of prominent lensing clusters around  $z_l \sim 1$  include those previously analyzed with HST data, such as MCXC J1226.9+3332 ( $z_l = 0.89$ ,  $\theta_{E,z_s=2} = 14.5 \pm 1.5$ , A. Zitrin et al. 2015), SPT-CL J0615-5746 ( $z_l = 0.97$ ,  $M(<200 \text{ kpc}) = 2.51_{-0.09}^{+0.15} \times 10^{14} M_\odot$ , R. Paterno-Mahler

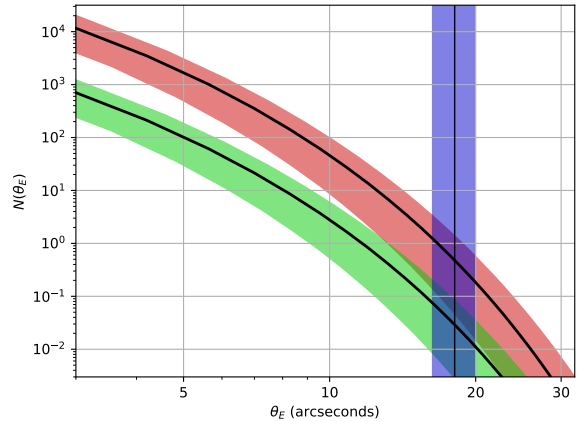


**Figure 4.** The expected distribution of Einstein radii around  $z_l \sim 1.07$  for a source at  $z_s = 3$ , across the sky (shaded red), and for the SPT survey region ( $2500 \text{ deg}^2$ ; shaded green), vs. the Einstein radius of SPT-CL J0546-5345  $\theta_E = 18.1 \pm 1.8$  (vertical blue shaded region), for the same source redshift. The (nominally,  $1\sigma$ ) scatter in the Einstein radius distribution was computed by probing clusters in the range  $z = 1\text{--}1.2$  and from the scatter in the adopted  $c$ – $M$  relation (for more details, see Section 4.3). As can be seen, clusters with such Einstein radii are expected to be rare at this redshift (see discussion in Section 4.3).

et al. 2018), SPT-CL J0356-5337 ( $z_l = 1.04$ ,  $\theta_{E,z_s=3} \simeq 14''$ , G. Mahler et al. 2020; G. Smith et al. 2025), and El Gordo (ACT-CL J0102-4915,  $z_l = 0.87$ ,  $M(<500 \text{ kpc}) = (8.3 \pm 0.3) \times 10^{14} M_\odot$ , J. M. Diego et al. 2023). These clusters exhibit similar strong-lensing properties or central mass as SPT-CL J0546-5345 and hint that SPT-CL J0546-5345 analyzed in this work, although expected to be rare for its redshift, is in fact quite common. Thanks to HST and JWST data in particular, it is now becoming evident that galaxy clusters at  $z_l \gtrsim 1$  can be sufficiently massive and concentrated to form prominent strong lenses, especially for higher-redshift sources.

Over 100 clusters were detected at redshifts of  $z \sim 1$  or above with the SPT (e.g., L. E. Bleem et al. 2015). Of these, about a couple dozen are included in the SLICE program, which is designed to study the cosmological evolution of the high-mass end of the halo mass function using strong lensing, over a redshift range from  $z \sim 1.9$  to  $z \sim 0.2$ —corresponding to about 8 Gyr of cosmic time. It will thus allow us to investigate whether these other high-redshift clusters exhibit similarly impressive lensing features as seen in SPT-CL J0546-5345 and how these evolve with cluster redshift.

## 5. Summary

In this work, we present the first strong-lensing model for the  $z = 1.067$  galaxy cluster SPT-CL J0546-5345, enabled thanks to new JWST/NIRCam observations from the SLICE survey, complemented by previous HST data. The cluster reveals as a very prominent gravitational lens. Using the LTM mass-modeling technique coupled with color information, we identify 16 sets (and candidates) of multiply imaged galaxies spanning, according to their photometry and the best-fit mass model, the redshift range  $\sim 2\text{--}6$ . The multiply imaged systems include various interesting features, such as a candidate sextuply lensed point source, which may be an AGN; various dusty galaxies at cosmic noon; an extremely magnified stretched arc; and a hyperbolic-umbilic configuration.

The conspicuous lensing features align well with the significant Einstein radius of the cluster,  $\theta_{E,z_s=3} = 18.1 \pm 1.8$  for  $z_s = 3$ , or

$\theta_{E,z_s=9} = 27.9 \pm 2.8$  for  $z_s = 9$ , and with its central projected mass density,  $M (<200 \text{ kpc}) = (1.9 \pm 0.3) \times 10^{14} M_\odot$ . These values are similar to some of the best-studied lensing clusters such as those previously studied (e.g., in the frameworks of the CLASH, Hubble Frontier Fields, or RELICS programs), even though the cluster is at a significantly higher redshift and thus seen at a significantly earlier cosmic time, where such prominent strong-lensing clusters are expected to be scarce. We compare this Einstein radius with the distribution of Einstein radii predicted for the cluster's redshift and find that it is indeed expected to be rare, in particular when taking into account the SPT survey area. According to our simplified estimation presented in Section 4.3, only a few clusters are expected to show equal or larger Einstein radii, at  $z \simeq 1\text{--}1.2$ , across the whole sky. Nonetheless, several other prominent lenses have been discovered around redshift  $z \sim 1$  in recent years, including those analyzed by C. Cerny et al. (2025) using similar JWST data from the SLICE survey.

This work thus highlights the advantage of using JWST, thanks to its sensitivity and wavelength coverage, in cluster evolution and lensing-related studies, and their extension to higher lens redshifts of  $z \gtrsim 1$ . Analysis of more  $z > 1$  clusters with JWST in the SLICE program is forthcoming.

### Acknowledgments

The authors thank the reviewer of this work for useful comments, which helped to improve the Letter. The authors would like to thank G. Brammer and the DAWN JWST Archive. A.Z. acknowledges support by grant 2020750 from the United States-Israel Binational Science Foundation (BSF) and grant 2109066 from the United States National Science Foundation (NSF), and by the Israel Science Foundation grant No. 864/23. M.J. is supported by the United Kingdom Research and Innovation (UKRI) Future Leaders Fellowship “Using Cosmic Beasts to uncover the Nature of Dark Matter” (grant No. MR/X006069/1). M.L. acknowledges CNRS and CNES for support.

This work is based on observations made with the NASA/ESA/CSA James Webb Space Telescope (JWST) and with the NASA/ESA Hubble Space Telescope (HST). The data were obtained from the Barbara A. Mikulski Archive for Space Telescopes (MAST) at the Space Telescope Science Institute (STScI), which is operated by the Association of Universities for Research in Astronomy (AURA), Inc., under NASA contract NAS 5-03127 for JWST. These observations are associated with the JWST GO program number 5594 and HST 12477, 15294. The HST specific observations analyzed can be accessed via doi:[10.17909/284j-8g39](https://doi.org/10.17909/284j-8g39), while the JWST data set is at doi:[10.17909/t661-kf88](https://doi.org/10.17909/t661-kf88). The maps associated to the lens model, as well catalogs cited in this Letter may be downloaded from the Zenodo data set doi:[10.5281/zenodo.16534337](https://doi.org/10.5281/zenodo.16534337).

### ORCID iDs

- Joseph F. V. Allingham <https://orcid.org/0000-0003-2718-8640>
- Adi Zitrin <https://orcid.org/0000-0002-0350-4488>
- Miriam Golubchik <https://orcid.org/0000-0001-9411-3484>
- Lukas J. Furtak <https://orcid.org/0000-0001-6278-032X>
- Matthew Bayliss <https://orcid.org/0000-0003-1074-4807>
- Catherine Cerny <https://orcid.org/0000-0002-8261-9098>
- Jose M. Diego <https://orcid.org/0000-0001-9065-3926>

- Alastair C. Edge <https://orcid.org/0000-0002-3398-6916>
- Raven Gassis <https://orcid.org/0009-0004-7337-7674>
- Michael D. Gladders <https://orcid.org/0000-0003-1370-5010>
- Mathilde Jauzac <https://orcid.org/0000-0003-1974-8732>
- David J. Lagattuta <https://orcid.org/0000-0002-7633-2883>
- Gavin Leroy <https://orcid.org/0009-0004-2523-4425>
- Marceau Limousin <https://orcid.org/0000-0001-6636-4999>
- Guillaume Mahler <https://orcid.org/0000-0003-3266-2001>
- Ashish K. Meena <https://orcid.org/0000-0002-7876-4321>
- Priyamvada Natarajan <https://orcid.org/0000-0002-5554-8896>
- Keren Sharon <https://orcid.org/0000-0002-7559-0864>

### References

- Abdulshafy, S., Abdullah, M. H., Wilson, G., Balogh, M. L., & Mabrouk, R. H. 2025, arXiv:[2505.12110](https://arxiv.org/abs/2505.12110)
- Acebron, A., Zitrin, A., Coe, D., et al. 2020, *ApJ*, **898**, 6
- Aguirre, P., Lindner, R. R., Baker, A. J., et al. 2018, *ApJ*, **855**, 26
- Andersson, K., Benson, B. A., Ade, P. A. R., et al. 2011, *ApJ*, **738**, 48
- Balogh, M. L., van der Burg, R. F. J., Muzzin, A., et al. 2021, *MNRAS*, **500**, 358
- Bertin, E., & Arnouts, S. 1996, *A&AS*, **117**, 393
- Bertin, E., Mellier, Y., Radovich, M., et al. 2002, in ASP Conf. Ser. 281, The TERAPIX Pipeline, ed. D. A. Bohlander, D. Durand, & T. H. Handley (San Francisco, CA: ASP), 228
- Bleem, L. E., Stalder, B., de Haan, T., et al. 2015, *ApJS*, **216**, 27
- Brammer, G., Strait, V., Matharu, J., & Momcheva, I. 2022 grizli, 1.5.0, Zenodo, <https://doi.org/10.5281/zenodo.6672538>
- Broadhurst, T., Benítez, N., Coe, D., et al. 2005, *ApJ*, **621**, 53
- Brodwin, M., Ruel, J., Ade, P. A. R., et al. 2010, *ApJ*, **721**, 90
- Bruzual, G., & Charlot, S. 2003, *MNRAS*, **344**, 1000
- Carnall, A. C., McLure, R. J., Dunlop, J. S., & Davé, R. 2018, *MNRAS*, **480**, 4379
- Carrasco, M., Zitrin, A., & Seidel, G. 2020, *MNRAS*, **491**, 3778
- Cerny, C., Mahler, G., Sharon, K., et al. 2025, arXiv:[2503.17498](https://arxiv.org/abs/2503.17498)
- Cloonan, A. P., Khullar, G., Napier, K. A., et al. 2025, *ApJ*, **987**, 194
- Coe, D., Salmon, B., Bradač, M., et al. 2019, *ApJ*, **884**, 85
- Diego, J. M., Meena, A. K., Adams, N. J., et al. 2023, *A&A*, **672**, A3
- Dressler, A., Bigelow, B., Hare, T., et al. 2011, *PASP*, **123**, 288
- Ebeling, H., Edge, A. C., Mantz, A., et al. 2010, *MNRAS*, **407**, 83
- Fox, C., Mahler, G., Sharon, K., & Remolina González, J. D. 2022, *ApJ*, **928**, 87
- Furtak, L. J., Mainali, R., Zitrin, A., et al. 2023a, *MNRAS*, **522**, 5142
- Furtak, L. J., Zitrin, A., Weaver, J. R., et al. 2023b, *MNRAS*, **523**, 4568
- Furtak, L. J., Labb  , I., Zitrin, A., et al. 2024a, *Natur*, **628**, 57
- Furtak, L. J., Zitrin, A., Richard, J., et al. 2024b, *MNRAS*, **533**, 2242
- Gladders, M. D., & Yee, H. K. C. 2000, *AJ*, **120**, 2148
- Gladders, M. D., & Yee, H. K. C. 2005, *ApJS*, **157**, 1
- Golubchik, M., Steinhardt, C. L., Zitrin, A., et al. 2024, *ApJ*, **976**, 108
- Hilton, M., Sif  n, C., Naess, S., et al. 2021, *ApJS*, **253**, 3
- Jauzac, M., Mahler, G., Edge, A. C., et al. 2019, *MNRAS*, **483**, 3082
- Ji, X., Maiolino, R.,   bler, H., et al. 2025, arXiv:[2501.13082](https://arxiv.org/abs/2501.13082)
- Kawamata, R., Oguri, M., Ishigaki, M., Shimasaku, K., & Ouchi, M. 2016, *ApJ*, **819**, 114
- Kravtsov, A. V., & Borgani, S. 2012, *ARA&A*, **50**, 353
- Lagattuta, D. J., Richard, J., Ebeling, H., et al. 2023, *MNRAS*, **522**, 1091
- Limousin, M., Beauchesne, B., Niemiec, A., et al. 2025, *A&A*, **693**, A33
- Lotz, J. M., Koekemoer, A., Coe, D., et al. 2017, *ApJ*, **837**, 97
- Mahler, G., Sharon, K., Fox, C., et al. 2019, *ApJ*, **873**, 96
- Mahler, G., Sharon, K., Gladders, M. D., et al. 2020, *ApJ*, **894**, 150
- Martizzi, D., & Agrusa, H. 2016, arXiv:[1608.04388](https://arxiv.org/abs/1608.04388)
- Meena, A. K., & Bagla, J. S. 2024, *OJAp*, **7**, 91
- Meneghetti, M., Bartelmann, M., & Moscardini, L. 2003, *MNRAS*, **346**, 67
- Meneghetti, M., Rasia, E., Merten, J., et al. 2010, *A&A*, **514**, A93
- Meneghetti, M., Rasia, E., Vega, J., et al. 2014, *ApJ*, **797**, 34
- Mu  oz-Echever  a, M., Macias-P  rez, J. F., Pratt, G. W., et al. 2024, *A&A*, **682**, A147
- Napier, K., Sharon, K., Dahle, H., et al. 2023, *ApJ*, **959**, 134
- Navarro, J. F., Frenk, C. S., & White, S. D. M. 1996, *ApJ*, **462**, 563

- Oke, J. B., & Gunn, J. E. 1983, *ApJ*, **266**, 713  
 Orban de Xivry, G., & Marshall, P. 2009, *MNRAS*, **399**, 2  
 Paterno-Mahler, R., Sharon, K., Coe, D., et al. 2018, *ApJ*, **863**, 154  
 Phuravathu, D. G., Hilton, M., Sikhosana, S. P., et al. 2025, *MNRAS*, **542**, 1544  
 Planck Collaboration, Aghanim, N., Arnaud, M., et al. 2011, *A&A*, **536**, A26  
 Planelles, S., Schleicher, D. R. G., & Bykov, A. M. 2015, *SSRv*, **188**, 93  
 Postman, M., Coe, D., Benítez, N., et al. 2012, *ApJS*, **199**, 25  
 Rasia, E., Meneghetti, M., Martino, R., et al. 2012, *NJPh*, **14**, 055018  
 Richard, J., Kneib, J.-P., Limousin, M., Edge, A., & Jullo, E. 2010, *MNRAS*, **402**, L44  
 Richard, J., Jauzac, M., Limousin, M., et al. 2014, *MNRAS*, **444**, 268  
 Rieke, M. J., Kelly, D. M., Misselt, K., et al. 2023, *PASP*, **135**, 028001  
 Ruel, J., Bazin, G., Bayliss, M., et al. 2014, *ApJ*, **792**, 45  
 Rykoff, E. S., Rozo, E., Busha, M. T., et al. 2014, *ApJ*, **785**, 104  
 Sadeh, S., & Rephaeli, Y. 2008, *MNRAS*, **388**, 1759  
 Schrabback, T., Applegate, D., Dietrich, J. P., et al. 2018, *MNRAS*, **474**, 2635  
 Sifón, C., Battaglia, N., Hasselfield, M., et al. 2016, *MNRAS*, **461**, 248  
 Smith, G., Mahler, G., Napier, K., et al. 2025, arXiv:[2507.07404](#)  
 Springel, V., White, S. D. M., Jenkins, A., et al. 2005, *Natur*, **435**, 629  
 Staniszewski, Z., Ade, P. A. R., Aird, K. A., et al. 2009, *ApJ*, **701**, 32  
 Steinhardt, C. L., Jauzac, M., Acebron, A., et al. 2020, *ApJS*, **247**, 64  
 Sweet, S. M., Sharp, R., Glazebrook, K., et al. 2017, *MNRAS*, **464**, 2910  
 Tinker, J., Kravtsov, A. V., Klypin, A., et al. 2008, *ApJ*, **688**, 709  
 Vanderlinde, K., Crawford, T. M., de Haan, T., et al. 2010, *ApJ*, **722**, 1180  
 Vanzella, E., Claeysens, A., Welch, B., et al. 2023, *ApJ*, **945**, 53  
 Watson, W. A., Iliev, I. T., Diego, J. M., et al. 2014, *MNRAS*, **437**, 3776  
 Williams, P. R., Treu, T., Dahle, H., et al. 2021, *ApJL*, **915**, L9  
 Wu, J. F., Aguirre, P., Baker, A. J., et al. 2018, *ApJ*, **853**, 195  
 Zalesky, L., & Ebeling, H. 2020, *MNRAS*, **498**, 1121  
 Zeldovich, I. B., Einasto, J., & Shandarin, S. F. 1982, *Natur*, **300**, 407  
 Zitrin, A., Broadhurst, T., Umetsu, K., et al. 2009, *MNRAS*, **396**, 1985  
 Zitrin, A., Meneghetti, M., Umetsu, K., et al. 2013, *ApJL*, **762**, L30  
 Zitrin, A., Fabris, A., Merten, J., et al. 2015, *ApJ*, **801**, 44  
 Zitrin, A., Seitz, S., Monna, A., et al. 2017, *ApJL*, **839**, L11